Explorations of the Annual Mean Heat Budget of the Tropical Indian Ocean. Part II: Studies with a Simplified Ocean General Circulation Model

RUI-JIN HU

Physical Oceanography Laboratory, and Ocean–Atmosphere Interaction and Climate Laboratory, Ocean University of China, Qingdao, China

J. STUART GODFREY

CSIRO Marine Research, Hobart, Australia

(Manuscript received 2 May 2005, in final form 11 July 2006)

ABSTRACT

Present-day OGCMs give low values of annual mean net heat flux (AMNHF) in the tropical Indian Ocean, compared to climatologies. AMNHF generation is examined in an open-boundary model of this region with realistic coastlines. In the first two of three experiments only annual mean wind stresses were applied so that a modified form of the "minimum depth criterion" of the previous paper would be applicable. Area-integrated AMNHF was well below observed values, despite the fact that western boundary inflow was substantially deeper and colder than was expected from the modified minimum depth estimate. The model showed large "spikes" in the gradient of "depth-integrated steric height" (DISH) along the western boundary, coinciding with coastline steps (which were absent in the previous paper). Most diapycnal entrainment occurred next to the coast, near these steps. In a third experiment a seasonal cycle of wind stress was added to the same annual mean. Annual mean diapycnal mixing and entrainment increased and the western boundary inflow deepened, resulting in substantially greater AMNHF for the same annual mean Ekman transports. However, area-integrated AMNHF was still well below the mean of directly observed surface fluxes. The recirculation around the "Great Whirl" doubled, permitting more cold water crossing the equator in one year to mix with recirculated water generated in a previous year. Entrainment up to the surface thus went by stages, over more than one year. The increased Great Whirl was related to stronger annual mean curls of nonlinear terms in the momentum equation, while the deeper entrainment was caused by stronger annual mean diapycnal mixing. In all experiments, diapycnal mixing was primarily due to the "flux corrected transport" (FCT) advective scheme, which in effect replaces spurious convective overturn by numerical diffusion. More research is needed to solve such problems, but sensitivity of AMNHF in OGCMs to time-varying forcing—due to seasonal, intraseasonal, or baroclinic instability—may offer a new source of climate predictability.

1. Introduction

In the previous paper (Godfrey et al. 2007, hereafter Part I) it was shown that observed annual mean net heat fluxes (AMNHFs) into the tropical Indian Ocean are much greater than those from present-day ocean general circulation models (OGCMs); see Fig. 1. This suggests that this region of the ocean may couple more strongly with the atmosphere than previously thought, with consequences for (e.g.) predictability of monsoons, or ENSO. It also means that, in the real Indian Ocean, a substantial part of the geostrophic inflow replacing southward Ekman transport must be colder than the minimum sea surface temperature (SST); this can only become part of the Ekman outflow if it is warmed by diapycnal processes. The low heat flux from the OGCMs means that they are not generating enough diapycnal mixing and entrainment below the minimum SST. An idealized version of the tropical Indian Ocean—a rectangular box with a steady and constant (southward) Ekman transport everywhere—was built to create a crude analog of the heat budget of the re-

Corresponding author address: Rui-Jin Hu, Physical Oceanography Laboratory, and Ocean–Atmosphere Interaction and Climate Laboratory, Ocean University of China, 266003 Qingdao, China.
E-mail: huruijin@ouc.edu.cn

DOI: 10.1175/JCLI4158.1

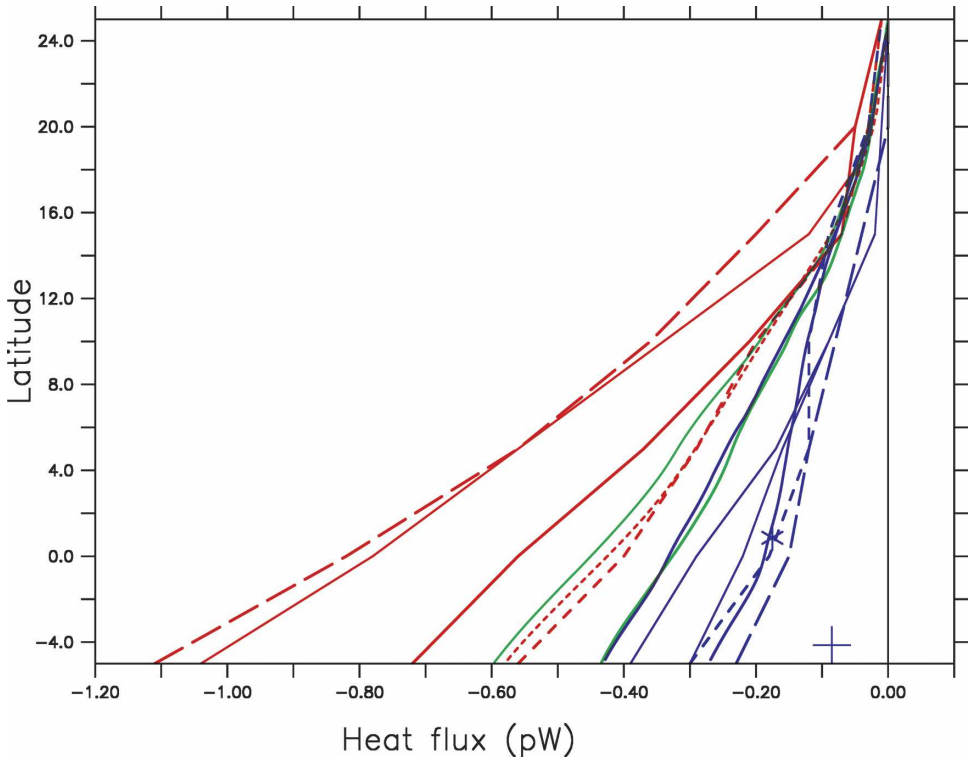

FIG. 1. This is basically a repeat of Fig. 1 of Part I. Red lines show the annual mean net heat flux north of latitude y in petawatts in the Indian Ocean, from observed climatologies. The dotted red line ending at 5°S, −0.58°W is from a climatology constructed for this paper. All other lines are estimates of annual mean net heat flux north of latitude y from various OGCMs. See text, and Table 1 of Part I, for details.

gion. The Ekman transport passed out through the open top 50 m of the southern boundary and was replaced by colder inflow through a full-depth "Indonesian gap." A zonal jet from this gap fed a north-flowing western boundary current, which fed upwelling at the northern boundary. Diapycnal mixing did occur in this model; it was confined to the strongly sheared currents around an eddy in the northwest corner of the rectangular model domain, which had qualitative similarities with the "Great Whirl" in the real Indian Ocean. Recirculation of water around the eddy allowed some of the upwelled water to warm by surface heat flux and then return around the eddy, where it was available for mixing with newer, unwarmed inflow. Some of the resulting mixture could then be warm enough to join the Ekman outflow.

The major simplifications made in building this model mean that it cannot be used to test whether this is or is not a useful analogy for the way water colder than minimum SST joins the southward Ekman transport in the real Indian Ocean. In this paper, five of the most obvious limitations of the model of Part I are addressed—unrealistic basin shape, annual mean wind stress, and surface heat boundary conditions, plus lack of seasonality of stress and of heat fluxes. In the first experiment of the present paper, the idealized basin shape and wind stresses of Part I were replaced with (a reasonable approximation to) the observed Indian Ocean coastline shape, and it was forced with observed annual mean winds and "swamp temperature" T_{swamp}. As explained below, T_{swamp} is the value of SST, for given atmospheric variables, for which net surface heat flux is zero. In a second experiment seasonality of T_{swamp} (only) was allowed for; and in a third, the observed seasonal cycle of variations was added to the annual means of both T_{swamp} and wind stress.

In these three experiments, the same rather coarse vertical grid resolution was used as in Part I, so the model mixing will be subject to the numerical problems discussed in Part I. In addition, the inevitable "staircase" shape of realistic coastlines in a finite-difference MOM-style model may cause further model problems. Nevertheless, new insights may be gained into whether or not the model version of the Great Whirl (and associated recirculating features) plays the same qualitative role as in Part I, that is, whether it allows incoming water, colder than the minimum SST, to warm up to minimum SST and join the Ekman outflow.

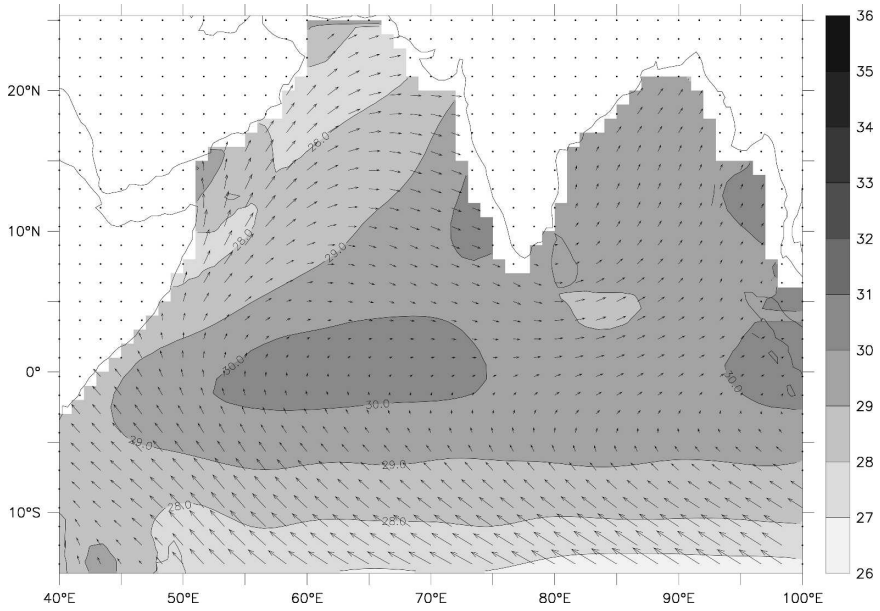

FIG. 2. The white areas indicate model "land"; the line over it shows the real coastline. Note the Indonesian gap between 10° and 7°S at the eastern boundary; the southern boundary at 14°S is also open above 50 m. The arrows indicate annual mean wind stresses from the FSU product. The contours and shades show the annual mean "swamp temperature" used in parameterizing the surface heat flux; it is calculated from COADS data.

2. Details of the model and the experiments

a. The model

The model is of Modular Ocean Model (MOM) architecture (Pacanowski 1995) and is similar to that used in Part I with two major exceptions. First, north of 7°S (the north edge of the entry point of the Indonesian Throughflow) the basin shape is a somewhat simplified version of the real Indian Ocean coastline (Fig. 2). The Red Sea and Persian Gulf are cut off (so there are no salty outflows from them), Sumatra and Malaysia are joined at 100°E, and Sri Lanka is omitted. Vertical walls were chosen for all coastlines, above a flat bottom at 3000 m. This ensured that the modal decomposition (used in Part I to qualitatively understand the early, linear phase of the response to steady wind stresses) was still valid. It also ensured that a modified version of the "minimum depth hypothesis" of Part I should be applicable once steady state was achieved in an experiment with steady wind stresses (see the appendix). As in Part I, the horizontal grid resolution was 0.333° by 0.333°, and the vertical grid interval (qualitatively similar to most others in Table 1 of Part I) increased from 10 m in the top 100 m to 280 m at the bottom. The same lateral viscosity (2000 $m^2\ s^{-1}$) was used as in Part I, giving a Munk width of 46 km. There was no bottom friction.

In the previous paper, possible regions of low Richardson number were inadequately resolved vertically, possibly due to the coarse vertical grid used (typical of most present-day ocean models), the coarseness of the horizontal grid, and the use of Laplacian horizontal friction rather than the eddy-permitting biharmonic friction. This may be why Pacanowski–Philander (PP) mixing (Pacanowski and Philander 1981) was a minor player in Part I, with most of the mixing being done by other, somewhat unphysical, mechanisms. The same coarse resolution was deliberately used in the present paper to explore the role of any similar problems in the present more "realistic" model. As in experiment 3 of Part I, the explicit horizontal diffusivity was set to zero. Thus the only explicit diapycnal diffusivity used was PP diapycnal mixing, but the flux-corrected transport (FCT) tracer advection scheme (e.g., Griffies et al. 2000) was applied to control spurious convective overturn. As explained in Part I, the FCT scheme is designed to counter a problem that arises in "level" models (as opposed to models whose interfaces are density surfaces), namely that when the Peclet number $|q|\Delta r/\kappa$ exceeds 2, spurious two-gridpoint noise can arise in the r direction ($r = x, y, z$); Δr is the grid interval and q is the velocity component in the r direction. In the vertical direction this noise can lead to spurious convective overturn.

As in Part I the basin south of 7°S was rectangular in shape with a full-depth gap between 7° and 10°S in the

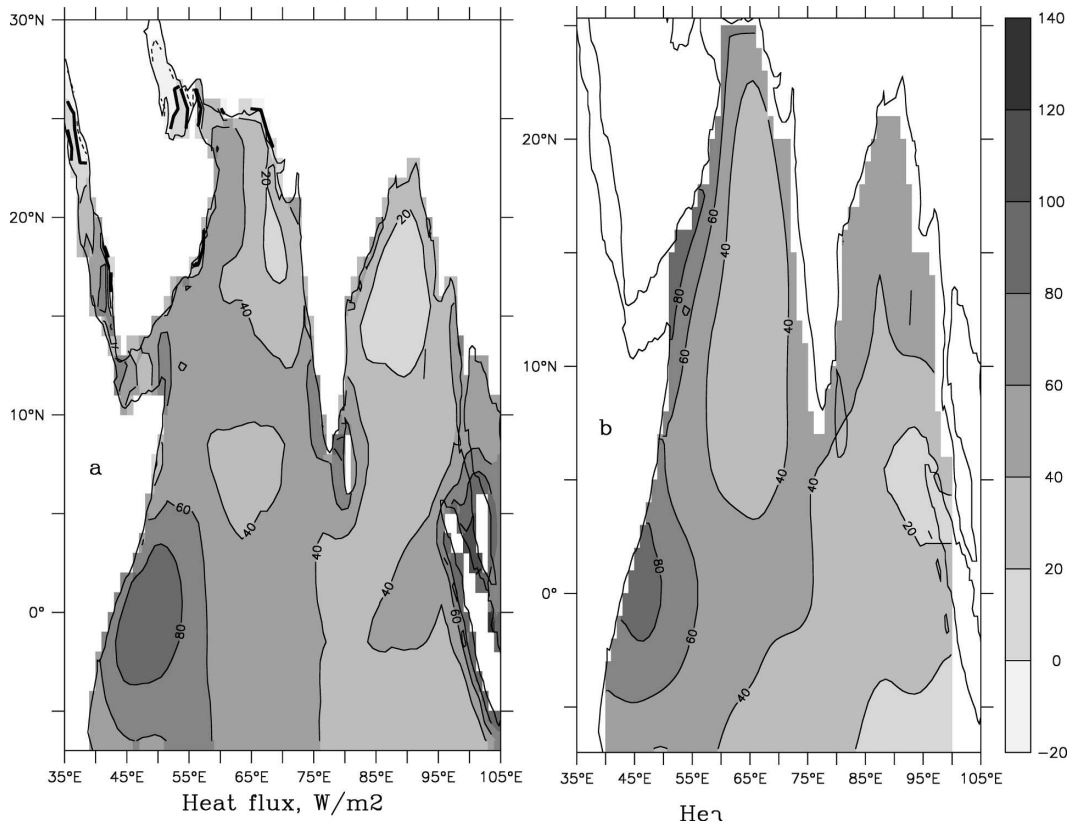

FIG. 3. (a) Annual mean net heat flux from Yu et al. (2004; see text). (b) As in (a) but from (2) (see text).

eastern boundary at 100°E and a gap in the top 50 m of the southern boundary at 14°S. The barotropic streamfunction at 14°S rose linearly eastward from zero at the western boundary to equal the instantaneous zonally integrated Ekman transport through 14°S. The eastern boundary streamfunction was constant at this value from 14° to 10°S, then fell linearly to zero from 10° to 7°S, across the gap at 100°E. Thus an equal and opposite barotropic inflow comes through the gap; this flow can be deeper and colder than the Ekman outflow through 14°S, requiring a net heat flux into the model domain in steady state.

The initial flow was zero with a horizontally uniform temperature profile set at each depth to the observed area-averaged annual mean temperature profile for the Indian Ocean north of 7°S (Levitus 1982). Salinity was 35 psu everywhere throughout all experiments.

The net surface heat flux was assumed proportional to the difference between the model SST and a swamp temperature T_{swamp} that is a function only of purely atmospheric variables. Comprehensive Ocean–Atmosphere Data Set (COADS) climatological observations (Da Silva et al. 1994) of wind speed, surface air temperature, and humidity (all purely atmospheric variables) were used along with the COADS estimates of net shortwave and longwave radiation R_s, R_l to calculate the seasonal cycle of T_{swamp} at each point. This is done by solving the equation

$$Q(\text{SST}) = R_s + R_l + LE(\text{SST}) + H(\text{SST}) = 0 \quad (1)$$

for that value $T_{\text{swamp}}(x, y, t)$ of SST for which the net heat flux Q(SST) would be zero (to within 1 Wm^{-2}), given all the other (purely atmospheric) variables. Here E and H are bulk formula estimates of the evaporation and sensible heat exchange, respectively, using a constant bulk transfer coefficient of 0.0015. The contours and shading in Fig. 2 show the annual mean values of T_{swamp} obtained in this way.

The surface boundary condition on the (downward) net heat flux Q is taken as a simple linear relation between Q and SST:

$$Q(\text{SST}) = dQ/d(\text{SST})|_{\text{SST}=T\text{swamp}}\,(\text{SST} - T_{\text{swamp}}). \quad (2)$$

In Part I, $dQ/d(\text{SST})|_{\text{SST}=T\text{swamp}}$ was chosen to be 15 $\text{W m}^{-2}\,^{\circ}\text{C}^{-1}$ in most experiments, for reasons explained there. In this paper the older value of 30 $\text{W m}^{-2}\,^{\circ}\text{C}^{-1}$ [typical of values suggested by Haney (1971) and Oberhuber (1988)] has been used; it led to a minimum SST that was approximately as observed.

Figure 3a shows the annual-mean net heat flux from

L. Yu et al. (2006, personal communication) averaged over 1988–99. The Yu et al. climatology (available from http://oaflux.whoi.edu) is largely based on satellite data—the International Satellite Cloud Climatology Project (ISCCP: e.g., Schiffer and Rossow 1983) dataset for longwave and shortwave radiation, plus their own, primarily satellite-based estimates of latent and sensible heat loss (Yu et al. 2004). Use of satellite data avoids the data gaps in other products where no merchant ship observations are available. For reasons discussed below another AMNHF product was generated from (2), using the observed SST from COADS (Fig. 3b). It is certainly not a reliable product for research purposes, but the two net heat flux estimates share important qualitative features. First, there are strong maxima in the annual-mean heat flux for several hundred kilometers offshore from the western boundary near the equator, with lesser maxima off Somalia and Arabia. Second, the annual-mean net heat flux is typically several tens of watts per square meter over most of the ocean basin north of 7°S—not just near boundaries. Quantitatively, the area integral of the climatological net heat flux estimate north of latitude y from (2) (dotted red line ending at 5°S, 0.58 PW in Fig. 1: 1 PW = 10^{15} W) lies near the lower end of the group of other climatologies, and in particular it is smaller in magnitude than the primarily satellite-based Yu et al. (2004) product, as can also be seen by comparing Figs. 3a,b. Nevertheless, the choice (2) of heat flux boundary condition ensures that, if the model generates AMNHFs that lie (say) 30 W m^{-2} below the climatological value of Fig. 3b, then the area-averaged, time-averaged SST returned by the model must also be significantly in error—it must lie above the COADS average (of 28.14°C) by 1°C.

b. The experiments

All three experiments described below were run for six years using the Florida State University (FSU) estimates of climatological wind stress for the period 1986–96 (Legler et al. 1989) over the area north of 14°S. In experiment 1, the first step from the idealized experiments of Part I toward realistic model conditions is made by driving it only with the steady, annual mean of the FSU wind stresses (vectors in Fig. 2) and the annual mean of T_{swamp}, also shown in Fig. 2. This experiment has realistic (annual mean) Ekman pumping and coastline shape.

Experiment 2 used the same annual mean wind stresses as in experiment 1 but the swamp temperature was replaced everywhere by its full seasonal cycle (contours in Fig. 4). Finally, in experiment 3, the full seasonal mean values of both wind stress (vectors in Fig. 4) and swamp temperature were used. This experiment is comparable in realism to others in Table 1 of Part I. The suite of experiments in Part I and the present work offer a new perspective on how surface heat fluxes may be controlled in the tropical Indian Ocean.

3. Basic results

a. Equilibration time

At the end of six years of running time, two indices suggested that the system was approaching equilibrium sufficiently well in each experiment (the meaning of "sufficiently well" will be discussed later in this subsection). These indices are shown in Figs. 5 and 6.

Figures 5a–c show the 12-month running mean (12MRM) "overturning streamfunction in temperature coordinates" $\psi(y, T, t)$ at $y = 5°S$, for experiments 1–3 (for ease of comparison a 12MRM is applied to all three experiments, even though it is unnecessary in experiment 1); $\psi(y, T, t)$ is the flow through latitude y above the T isotherm at time t. Comparing Fig. 5 with Fig. 6 of Part I, it seems that the equilibration time is considerably longer in the present situation where coastline geometry and winds are more realistic. The streamfunction is approaching equilibrium but still changing significantly with time at 6 yr in all three experiments. Near the end of the experiments, the minimum value of the streamfunction is at ~24°C in all three experiments; but it is ~5 Sv (Sv ≡ 10^6 m^3 s^{-1}) in experiments 1 and 2 and about 8 Sv in experiment 3.

The long-dashed and short-dashed red lines at the bottom of Fig. 6 show the 12MRM area-integrated net heat flux north of 5°S as a function of time in experiments 1 and 2, respectively, while the full red line is the same quantity for experiment 3. The long-dashed and short-dashed blue lines converging toward the net heat fluxes for experiments 1 and 2 are the 12MRM heat transports for those experiments. The solid blue line shows the 12MRM heat transport in experiment 3; it converges toward the area-integrated heat flux of experiment 3. Assuming that the final steady-state heat flux in each experiment is bounded below by the heat flux at year 6 and above by the heat transport at year 6, the final equilibrium heat flux is about 0.29 ± 0.02 pW for experiments 1 and 2 and 0.45 ± 0.02 pW in experiment 3. These numbers place the model area-integrated AMNHF at 5°S for experiment 3 at the upper edge of the group of OGCM results in Table 1 of Part I (apart from OFES2), while those for experiments 1 and 2 are well within the group. The heat flux at all latitudes at this time for experiments 2 and 3 are shown by the heavy purple lines in Fig. 1; the larger magnitudes come from experiment 3.

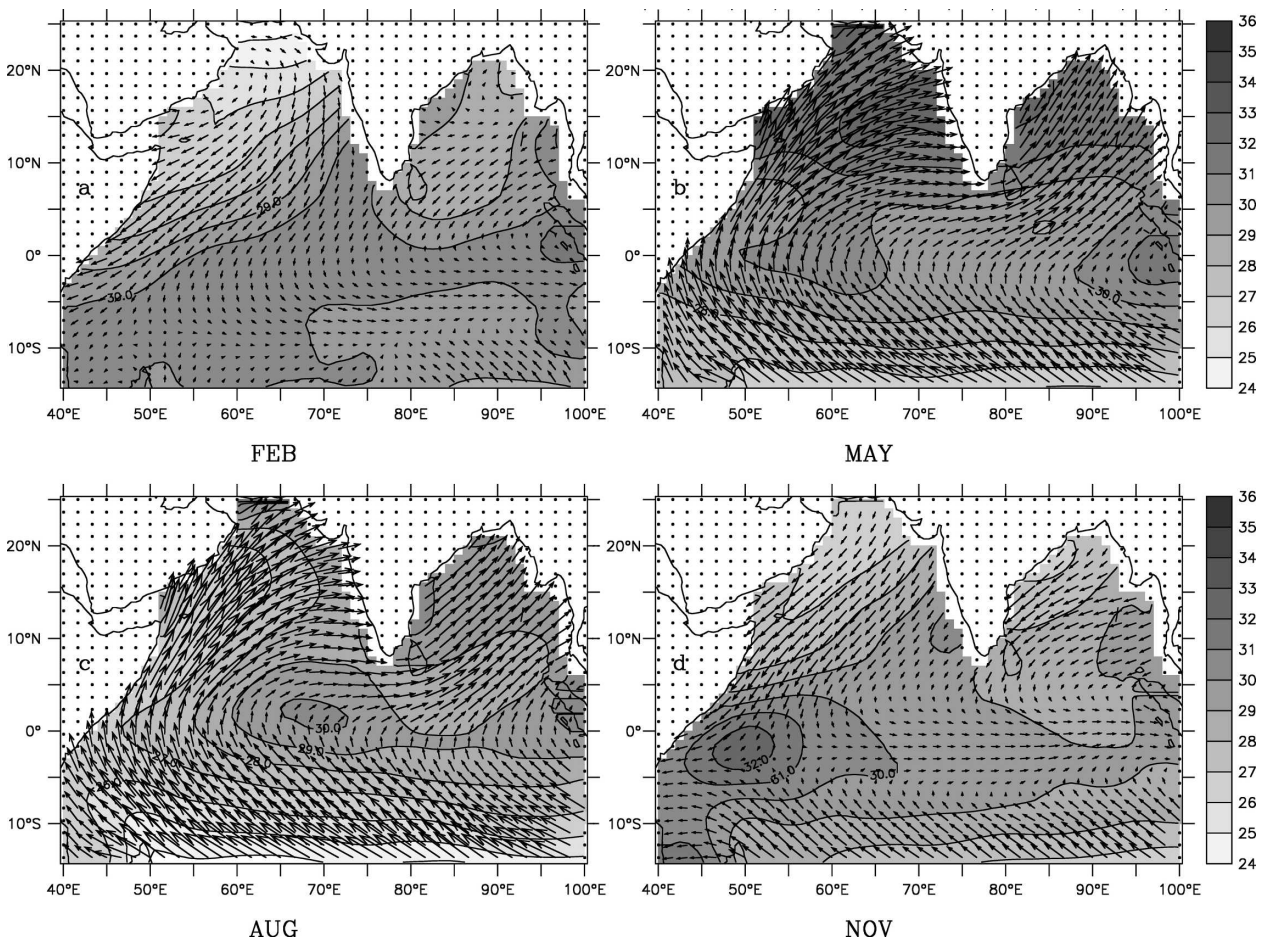

FIG. 4. Wind stresses (vectors) and swamp temperature (contours) for (a) February, (b) May, (c) August, and (d) November.

b. 12MRM heat flux in experiments 2 and 3

As can be seen in Figs. 5 and 6 and confirmed by other comparisons, there are few differences (on 12MRM) between the results of experiments 1 and 2. From now on—with one exception—experiments 2 and 3 only are compared (because they have identical heat flux boundary conditions and differ only in the wind stress pattern used). The exception occurs when discussing the "minimum depth" concept (section 4a below), which should only be valid for experiments with purely steady forcing and steady resulting flow. In this case experiment 1 is used.

Figures 7a,b show the annual mean heat flux for year 6 for experiments 2 and 3. The area-integrated AMNHF north of latitude y (thick purple lines in Fig. 1) is considerably greater in magnitude in experiment 3 (more negative purple line) than experiment 2. This is to be expected on the basis of appendix A of Part I in which it was concluded that an increase in annual mean heat flux can only occur through an annual mean increase in diapycnal diffusion. The diapycnal diffusive heat flux $-\kappa\partial T/\partial z$ is downward everywhere, and κ (at least for PP mixing) depends on the square of velocity shear. Therefore, when the intense seasonal flows are added to the annual mean, the annual mean value of κ (and resulting surface heat fluxes) is likely to increase through the rectification mechanism described by Lee and Marotzke (1998). Note that AMNHF is indeed higher nearly everywhere in Fig. 7b relative to Fig. 7a. However, except near the western boundary, both model-based estimates are generally weaker than the mean heat flux from the climatology of Fig. 3b.

This is seen in Fig. 7c, which shows the difference of the annual mean SST over year 6 of experiment 3 from the COADS observations. Because of the boundary condition in (2), Fig. 7c can also be regarded as the difference in heat flux between Figs. 3b and 7b divided by 30 W m^{-2} °C^{-1}. The heat flux of Fig. 3b was obtained from (2) with observed COADS atmospheric and SST data. Figure 7b is obtained in exactly the same way but

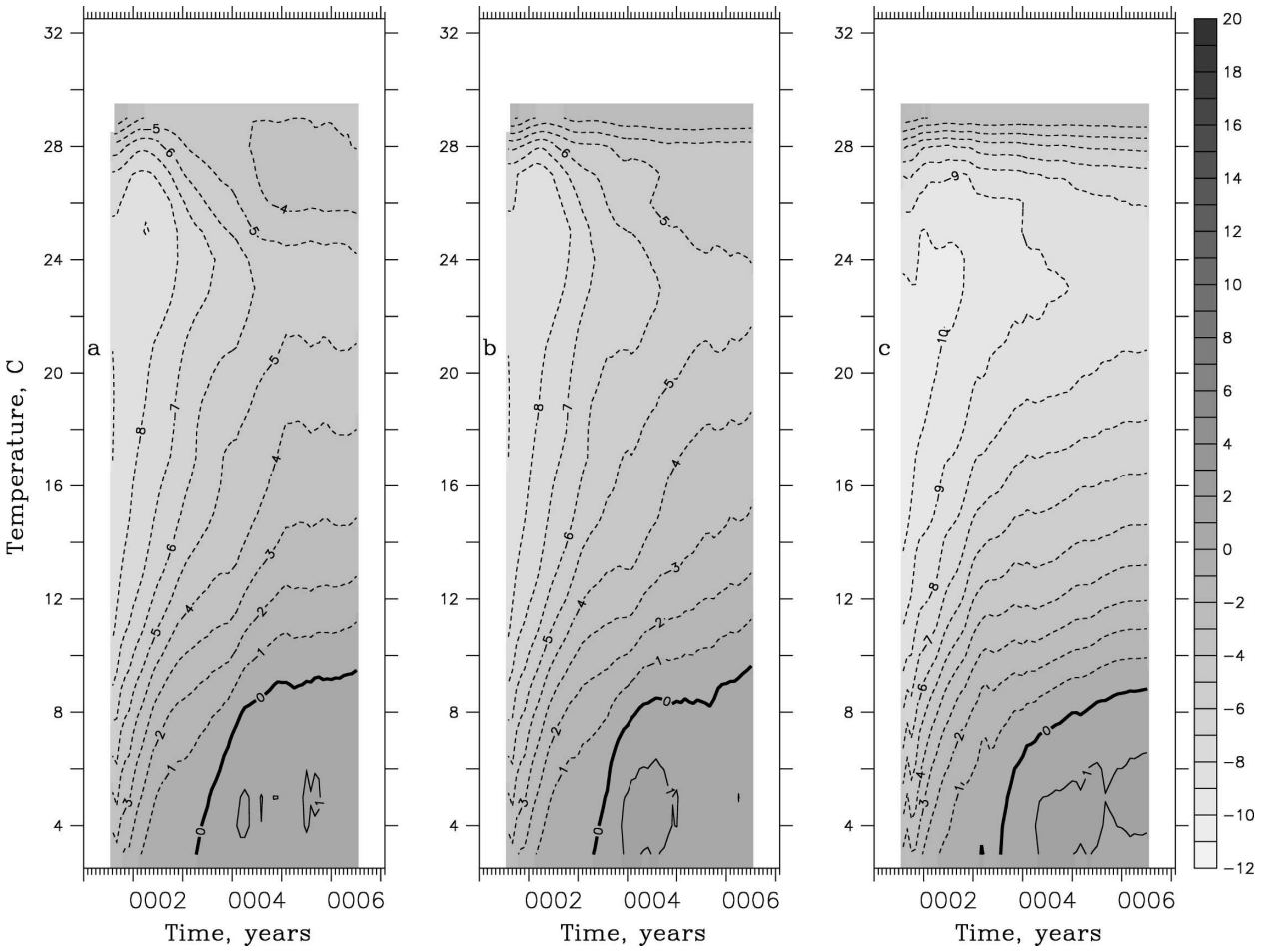

FIG. 5. The 12MRM overturning streamfunction in temperature coordinates through 5°S as a function of time and temperature, in experiments (a) 1, (b) 2, and (c) 3. Contour interval: 1 Sv.

with SST generated, instead, by the present model. The model SST is, in fact, too cool opposite Somalia—but too warm over the bulk of the ocean. The magnitudes of these SST errors (>0.5°C over most of the east Indian Ocean) are much greater than reasonable observational error estimates for annual mean SSTs. This picture highlights the fact that annual mean SST and heat flux are tightly related through (2); errors in heat flux are not "caused" by errors in SST. Rather, errors in both are caused simultaneously by errors in model physics. These errors may be due to numerical problems with simulating diapycnal diffusivity, the absence of the "storminess" supplied by daily wind forcing, or the lack of time-dependent eddies in our model.

c. *12MRM overturning streamfunction in temperature coordinates in experiments 2 and 3*

Figures 8a,b show the 12MRM overturning streamfunction in temperature coordinates for year 6 of experiments 2 and 3 respectively, as functions of latitude and temperature.

The maximum magnitude of the streamfunction at 5°S is seen to be 5 Sv, near 24°C, in Fig. 8a, and over 8 Sv, at 24°C, in Fig. 8a. Both streamfunctions are compatible with the Levitus (1987) picture of the heat transport being carried by the (annual mean) Ekman transport and the equal and opposite geostrophic flow. However, the maximum streamfunctions in Figs. 8a,b are both substantially less than the annual mean southward Ekman transport of 13 Sv (with the FSU winds). This must be because, due to the time-varying swamp temperatures in experiment 2, the annual mean Ekman transport (always southward) occurs over a wide range of temperatures; there is considerable cancellation between it and the oppositely directed geostrophic flow in the same temperature range. The stronger streamfunction values in Fig. 8b compared to Fig. 8a occur because the geostrophic inflow is colder and deeper in Fig. 8b, so there is less overlap with the Ekman transport.

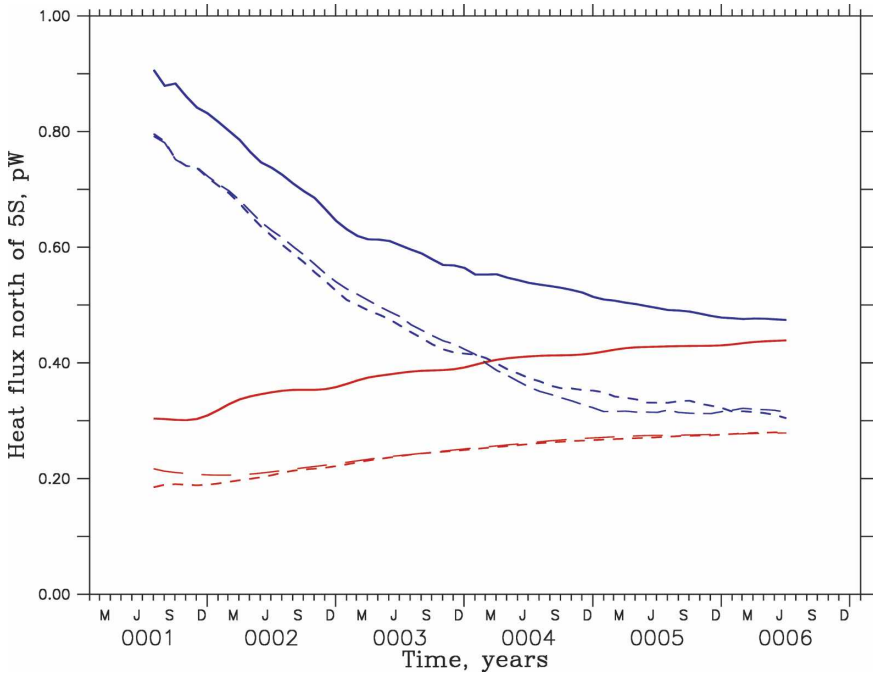

FIG. 6. The two long-dashed and short-dashed lines show the 12MRM area-integrated net heat flux north of 5°S as a function of time in experiments 1 and 2, respectively. The solid red line is the same quantity for experiment 3. The long-dashed and short-dashed lines converging toward the net heat fluxes for experiments 1 and 2 are the 12MRM heat transports for those experiments. The solid blue line shows the 12MRM heat transport in experiment 3. In equilibrium, the red and blue lines should coincide for each experiment. The experiment was stopped when the difference (i.e., the time-dependent term in the heat budget) was less than 10% of the total heat flux.

As discussed in the introduction of Part I, it would be useful to obtain a breakdown by temperature of the time-averaged streamfunctions into an Ekman and a geostrophic part, both of magnitude V_{Ek}; the "transport-weighted temperature"

$$\int_0^{30} \left(T \frac{\partial \psi_{geo}}{\partial T} \right) dT / V_{Ek}$$

of the geostrophic flow needed to be as cold as ~11°C if the heat transport was to be as large as suggested by observed climatologies. Unfortunately, it is not easy to make this breakdown: the zonal pressure gradients that balance the geostrophic meridional flow must be evaluated along isopycnals before zonally integrating them, and the result averaged over time. This has not been attempted. However, assuming that the Ekman flow is confined above 24°C and that quite strong northward geostrophic flow occurs above this temperature, it is most unlikely from inspection of Fig. 8 that the transport-weighted temperature of the geostrophic flow is nearly as low as 11°C, either in experiment 2 or 3.

Even in the case of the steady wind stresses of experiment 2, there is a large qualitative difference between Fig. 8a and the corresponding result in the idealized model (Fig. 7c of Part I). In the idealized model, the water flows more or less adiabatically along the western boundary until it upwells (in temperature space) into the Ekman layer near the northern boundary. In the present case with realistic topography and winds, this should not happen because wind-driven upwelling occurs all along the western boundary (north of the equator). However, this cannot explain all of the differences. The annual mean FSU winds of Fig. 2 drive only downwelling along the western boundary south of the equator; yet Fig. 8a shows upward entrainment of 2 Sv or more south of the equator for temperatures as low as 20°C—well below the minimum surface temperature of 26°C. This puzzling result will be discussed in section 4.

It has already been shown (Fig. 6) that by year 6 the total 12MRM heat transport through 5°S, from the overturning streamfunctions in Fig. 8, is close to the area integral, north of 5°S, of the heat fluxes of Fig. 7. Thus the stronger, deeper overturning circulation of Fig. 8b compared to Fig. 8a is consistent with the stron-

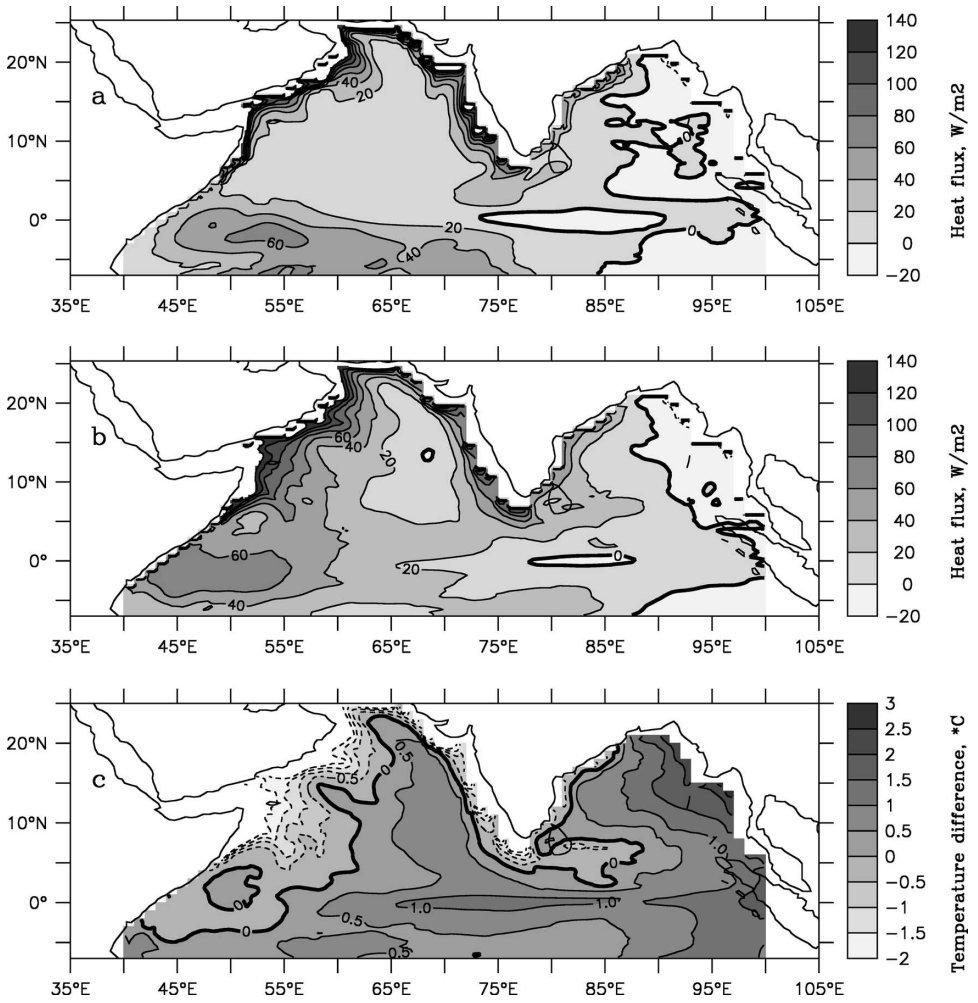

FIG. 7. Annual mean net heat flux for year 6 of (a) experiment 2 and (b) experiment 3. Contour interval: 20 W m^{-2}. (c) Difference between annual mean temperature in year 6 of experiment 3 and COADS observed values. Contour interval: 0.5°C.

ger heat flux of Fig. 7b compared to Fig. 7a. Both are consistent (through appendix A of Part I) with increased annual mean values of diapycnal diffusivities κ in experiment 3 compared to experiment 2, presumably due to the more strongly nonlinear flows of experiment 3.

d. Horizontal streamfunction

Figure 9a shows the horizontal streamfunction from the Sverdrup relation for the annual-mean wind stresses in Fig. 2. Figures 9b,c show the annual-mean horizontal streamfunction for year 6 of experiments 2 and 3. In all three panels of Fig. 9, the maximum value of the streamfunction on the equator lies near 46°E, just east of the western boundary current, and has a value of 10 ± 1 Sv—close to the annual mean "Ekman–Sverdrup" cross-equatorial transport (Miyama et al. 2003; Godfrey et al. 2001) obtained by integrating $(-1/\rho\beta)\partial\tau^{(x)}/dy$ across the basin at the equator for FSU winds (see Fig. 3 of Part I). A further feature the three experiments have in common is that the saddlepoint near 4°N separating the main gyre from the Great Whirl-like feature north of 4°N is near 5 Sv in all panels. Thus (at least on depth integral) some of the cross-equatorial western boundary flow penetrates only a few degrees north of the equator before returning south, while the rest circulates around the Great Whirl.

However, there are important differences between the panels. The sharp U-turn seen near 5°N, 70°E in Fig. 9a is smoothed in Fig. 9b, presumably due to the action of lateral friction. This is absent from the Sverdrup calculation. On the other hand, about half the western boundary flow recirculates southward across

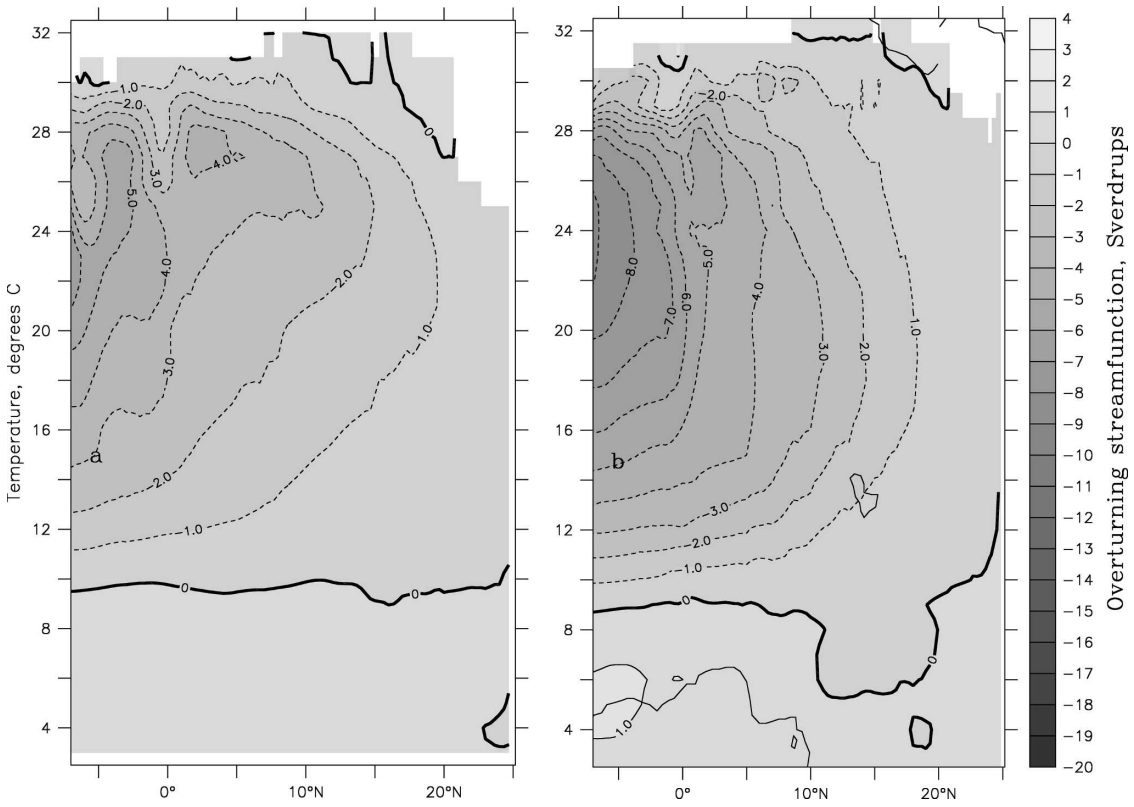

FIG. 8. The 12MRM overturning streamfunction in temperature coordinates for year 6 of experiments (a) 2 and (b) 3. Contour interval: 1 Sv.

the equator in Fig. 9b near 48°E. This is probably due to the fact that the outer streamlines of the western boundary current are too far from the boundary to pass their vorticity effectively to it, via lateral friction. Therefore (at least below the surface mixed layer where vorticity input from the wind stress curl cannot directly affect it) the equatorial vorticity barrier forces this flow to return south of the equator, in experiment 2. The linear model of Fig. 9a does not include the (nonlinear) effect of vorticity advection, so this recirculation effect cannot occur.

Figure 9c is markedly different again from Fig. 9b. The Great Whirl near (7°N, 52°E) is about twice as intense in experiment 3 (Fig. 9c) than experiment 2 (Fig. 9b). The recirculation across the equator has largely disappeared in Fig. 9c so that half the western boundary flow exits smoothly eastward along the equator (on annual average). It is joined in 55°–60°E by the 5-Sv outflow from around the Great Whirl and in 60°–80°E by a further 2 Sv emanating from the Bay of Bengal (this outflow is substantially weaker in Fig. 9b). As a result, the annual mean jet along the equator is stronger in Fig. 9c than in Fig. 9b at 80°E.

4. Some questions raised by these results

a. Is the minimum-depth concept useful for realistic topography and winds?

Appendix B of Part I considered the usefulness of a "minimum depth" concept for estimating the depth (and temperature) of the northward geostrophic inflow that replaces the southward Ekman flow. The appendix of the present paper derives a similar principle for experiments with arbitrary (vertical walled) basin shape and (steady) winds, such as experiment 1 and perhaps also experiment 2. (The rest of this subsection refers to experiment 1 since—with its steady winds and thermal forcing—it is most comparable to the results of Part I.) However, as already noted, Fig. 8 of this paper shows that entrainment through isotherms that lie below the coldest surface temperature is not confined to a location near the separation point of the western boundary, as it was in the experiments of Part I.

Figures 10 and 11 shed some insight on why this occurs. Depth-integrated steric height (DISH)—which is basically the field that provides geostrophic balance for depth-integrated, geostrophic flow—plays a central

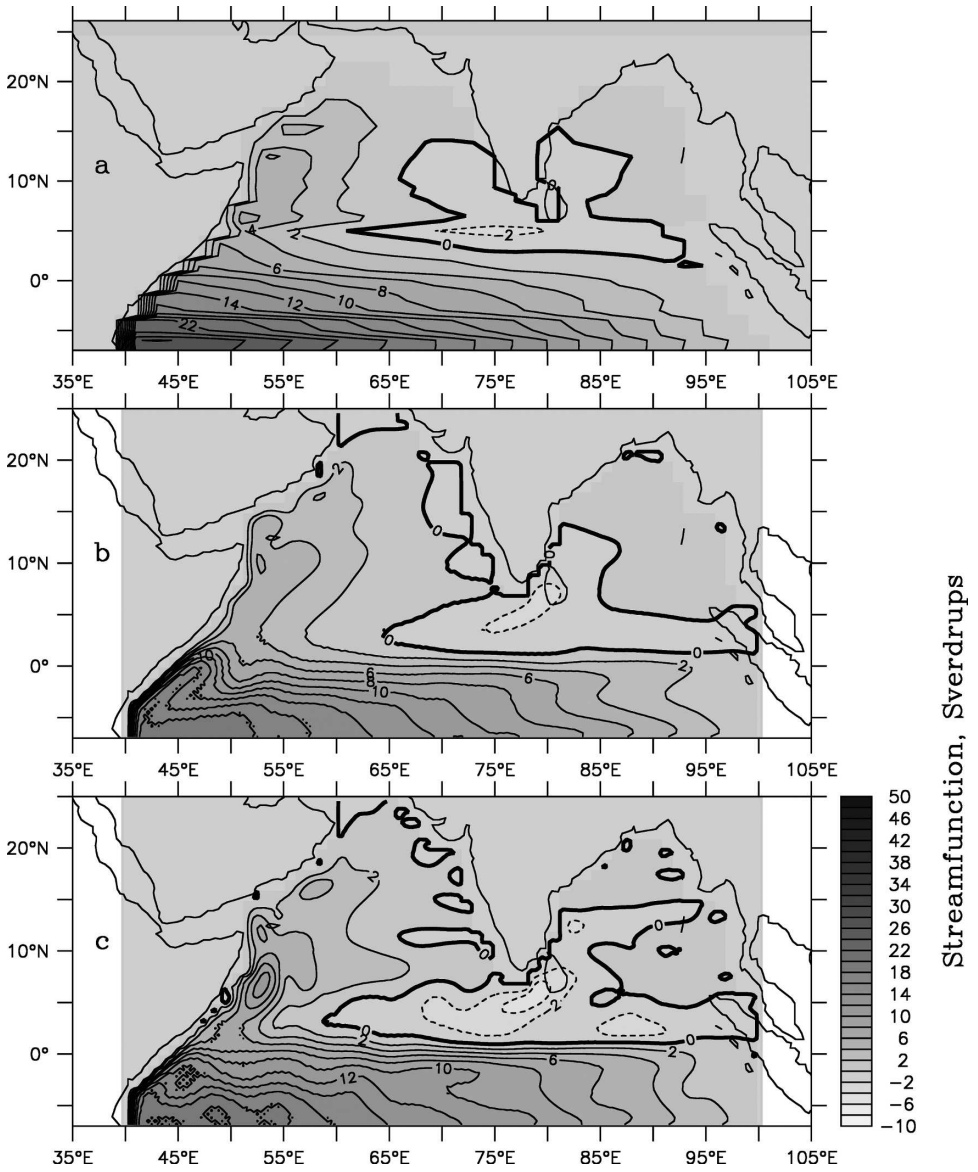

FIG. 9. (a) Sverdrup streamfunction for the FSU winds. Horizontal streamfunction averaged over the sixth year of integration for experiments (b) 2 and (c) 3. Contour interval: 2 Sv.

role in the minimum-depth hypothesis. As outlined in the appendix, a Sverdrup estimate of DISH can be obtained for any distribution of steady wind stress, and in particular for that of Fig. 2. Figure 10a shows this Sverdrup distribution; an additive constant has been applied to bring DISH to zero on the equator opposite Sumatra. Figure 10b shows DISH calculated from the model density field relative to an assumed depth of no motion at 1000 m averaged over year 6 of experiment 1; an additive constant is again applied to bring DISH to zero off Sumatra. According to the appendix, the minimum depth can be determined through (B3) or (B3′) of Part I from the DISH along the western boundary relative to the Sumatran coast. Figure 11a shows this quantity, from Fig. 10a; the average DISH over year 6 of experiments 2 and 3 is also shown.

There is good agreement between the broad features of the three estimates of DISH along the western boundary. All show a shallow minimum of DISH difference Δ(DISH) (relative to zero off Sumatra) of about –15 m^2 near 8°–10°N, implying deepest minimum depth there. The total geostrophic flow V through the entire integration path (shown in Fig. 16) is equal and opposite to the total Ekman transport through it (including sections along coastlines). Ignoring the small, but poorly determined, Ekman flux along the Sumatran

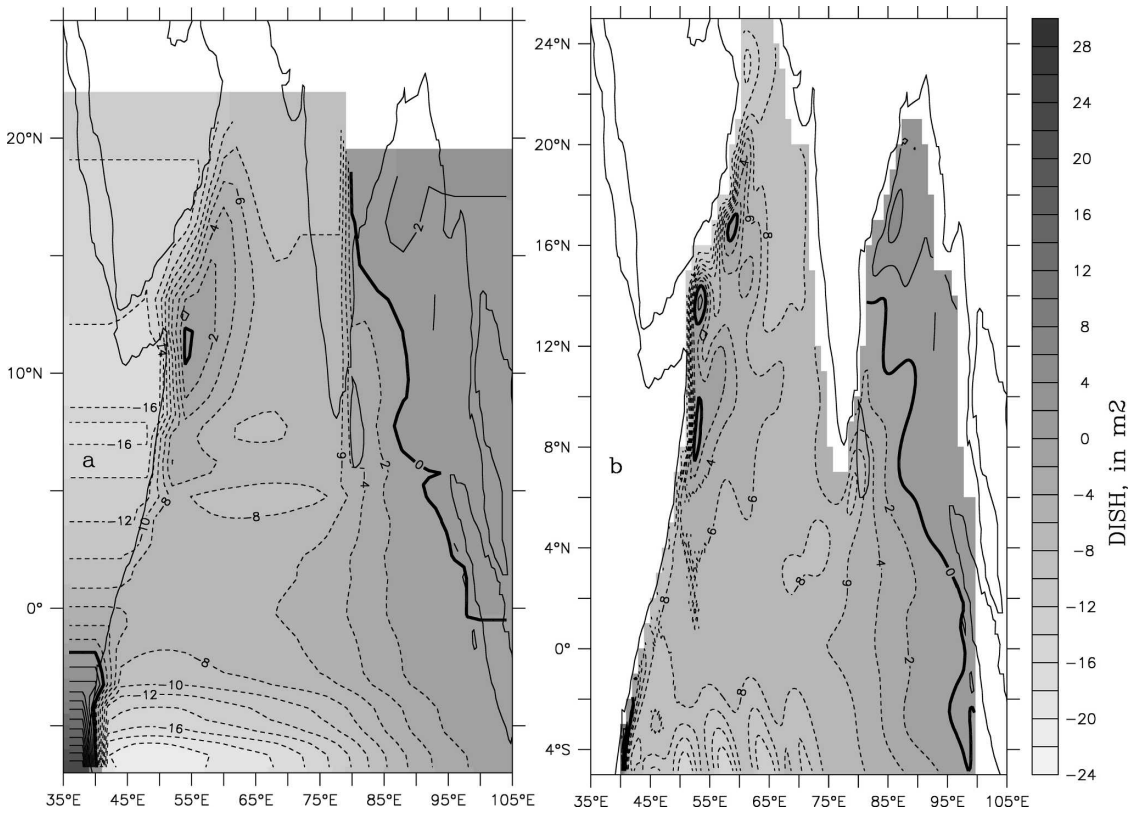

FIG. 10. (a) Depth-integrated steric height calculated for the model region of interest using the Sverdrup relation and geostrophy, as in the appendix. (b) The same quantity from experiment 1, calculated as $\int_z(\Delta(z)/\rho_0)\mathrm{d}z$ from 1000 m to the surface.

coast, this is about $V = g\Delta(\mathrm{DISH})/f(8°\mathrm{N}) = 7.8$ Sv. The average of the squared Brunt–Väisälä frequency N^2 in the top 158 m opposite Sumatra at the end of experiment 1 is 0.000 30 s^{-2}, giving an approximate minimum depth estimate via (B3′) of (Part I's appendix B) of $(6g\Delta(\mathrm{DISH})/N^2)^{1/3}$, or 143 m. The temperature at 143 m at the end of experiment 1 is about 14.5°C off Sumatra.

If (by analogy with experiment 3 of Part I) all flow north of the equator were confined above this minimum depth, then all flow would be confined to temperatures above 14.5°C. In fact, Fig. 8a shows 2 Sv crossing the equator with temperature between 10° and 14.5°C, in experiment 2; the same occurs in experiment 1. Why does the minimum-depth principle estimate the minimum flow temperature fairly accurately in experiment 3 of Part I but not in the present experiment with more realistic winds and topography?

According to Fig. 11a the model shows greatly enhanced alongshore gradients of DISH at some locations (e.g., 2°–3°S) compared to the Sverdrup values; the locations are the same in all three experiments, though the magnitudes differ. Such large gradients, which cannot be balanced geostrophically since they lie along the boundary, are likely to be sites of strong dynamic activity: they may be sites of strong upwelling (or downwelling) at which the Peclet number is likely to be large so that FCT instability might be expected. Figure 11b shows an expanded view of the DISH distribution, in experiment 2, along the African coast (red contours). The superposed shades and black contours show heat flux due to FCT mixing through the 17°C isotherm. Intense mixing maxima occur along the flanks of each "step" in the coastline. These tend to be stronger when there is also a strong alongshore gradient of DISH. Equivalent mixing events did not occur in the smooth-walled geometry of Part I. Thus, in the present model—and perhaps in others—boundary "steppiness" may influence where diapycnal mixing occurs. The results of Part I suggest that this steppiness effect may seriously distort the spatial distribution of mixing in the present model.

b. *What is the thermodynamic role of the enhanced Great Whirl in experiment 3?*

The flows in experiment 2 are essentially steady, and the streamfunction in Fig. 9b shows almost no closed

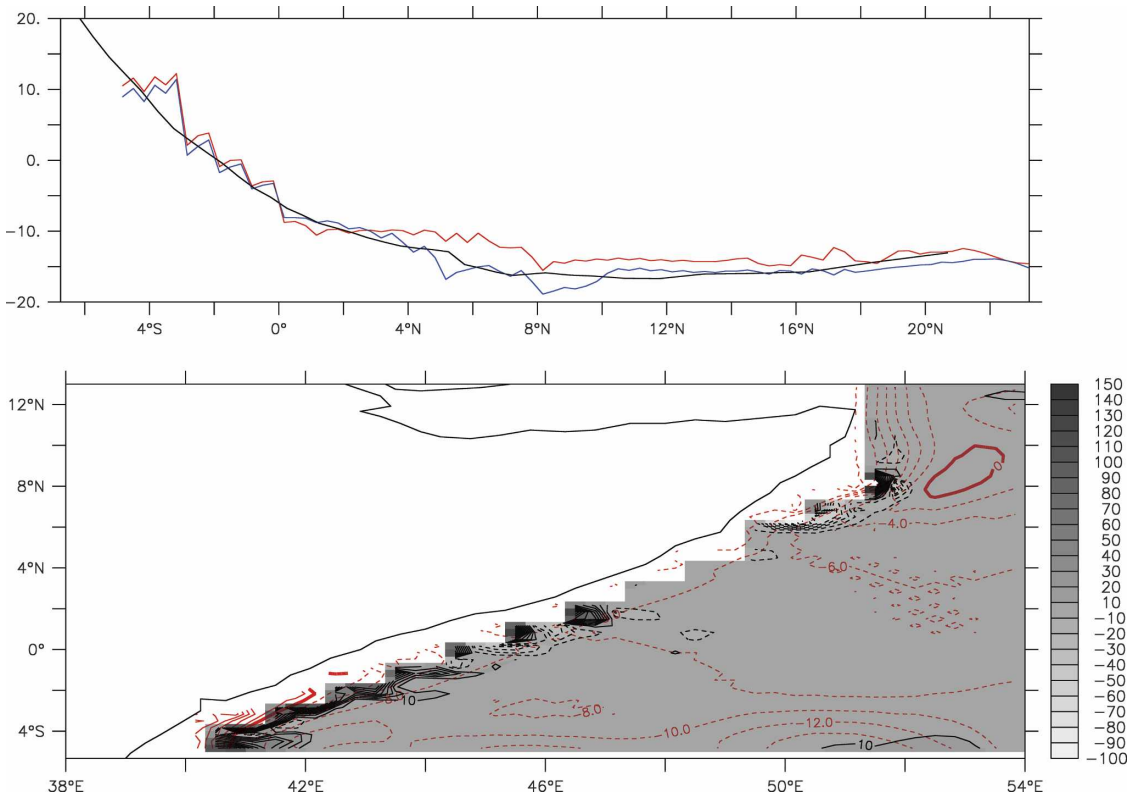

FIG. 11. (a) The solid line shows the DISH value along the western boundary of the Arabian Sea from the Sverdrup calculation of Fig. 10a (heavy solid line); and the corresponding values from experiments 1 (red) and 3 (blue) averaged over the final year. (b) Shading and contours near the model western boundary show the heat flux due to FCT mixing, at the end of experiment 1. Contours in red show details of the DISH field of Fig. 10b.

contours north of 5°N; so, in some average sense, it is only possible for a given flow particle to pass once around the Great Whirl. This is no longer necessarily true in experiment 3 when strong seasonal variations in currents occur. Comparison of Figs. 9b,c show that the Great Whirl is about twice as strong in experiment 3 as in experiment 2; in some average sense, then, water particles must pass around the Great Whirl twice before exiting in experiment 3.

By analogy with Part I, the extra passage around the whirl may permit diapycnal mixing and upward entrainment to be stronger and extend deeper in experiment 3, as is required to permit the colder, deeper inflow across the equator to escape southward in the surface mixed layer. When water with temperature less than (say) 15°C crosses the equator in the western boundary current (primarily in summer), it is trapped north of the equator by the equatorial vorticity barrier and can only return southward if it entrains upward through isothermal surfaces until it can reach the surface and be exposed to surface heating.

To illustrate this, Fig. 12a shows depth-integrated flow vectors below the 15°C isotherm, averaged over the final year of experiment 3 (arrows). The divergence of these vectors contains a great deal of two-gridpoint noise. To smooth this noise locally this divergence is integrated eastward in longitude starting from zero over land; only the average of adjacent grid points in y is plotted. The result (shading in Fig. 12a) may be thought of as the net downward entrainment, west of a given point, through 15°C. Strong zonal negative gradients of this net downwelling imply strong upward entrainment. Using this fact, inspection of Fig. 12a shows that the bulk of the upwelling and entrainment occurs within a few grid points of the western boundary between 0° and 8°N (consistent also with the peaks in FCT heat flux in Fig. 11b). Furthermore, bands of upwelling are aligned with coastline "corners."

The quantity of upwelling is comparable to the magnitude of the inflow itself: 4.6 Sv enters the region of Fig. 12a across the equator, mostly near the western boundary; 1.2 Sv escapes eastward across 70°E; and 0.3 Sv passes northward through 20°N. Thus 3.1 Sv—the bulk of the 4.6 Sv inflow—must entrain upward. Note that this 3.1 Sv is somewhat less than the value of the difference in overturning streamfunction between 0°

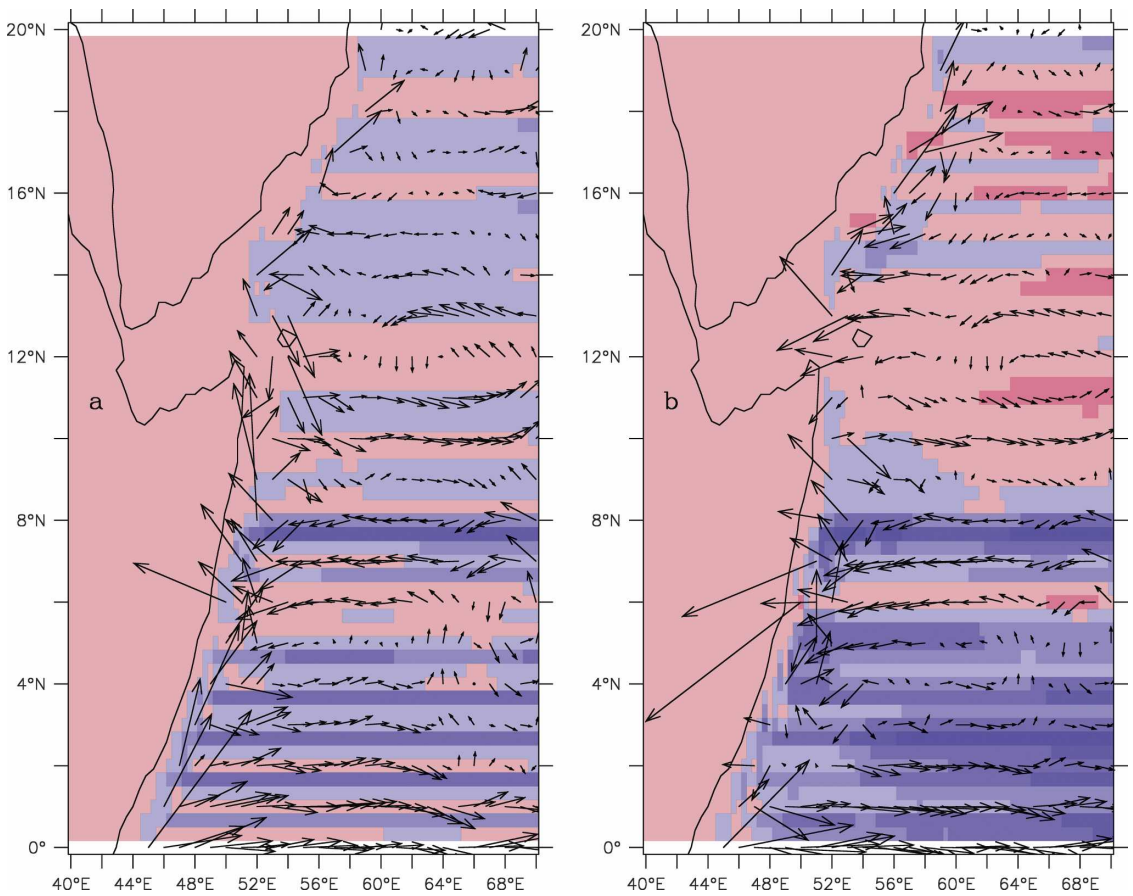

FIG. 12. The vectors show (a) the vertically integrated 12MRM flows in the region 0°–20°N, 40°–70°E below the 15°C isotherm, in experiment 3, and (b) the flows above the 26°C isotherm. The colors show the eastward integral of entrainment due to FCT mixing (a) through the 15°C isotherm and (b) through the 26°C isotherm.

and 20°N at 15°C in experiment 3 (about 4.5 Sv, according to Fig. 8b), due possibly to overturning in the Bay of Bengal.

A similar pattern emerges from examining the divergence of the flows, in experiment 3, above the 26°C isotherm (Fig. 12b); this isotherm is close to the minimum SST of 26°C in experiment 3. The inflows to the region through the south, east, and north boundaries are 1.2 Sv, −3.6 Sv, and –2.1 Sv, respectively, implying that the net outflow of 5.7 Sv across the eastern and northern boundaries is generated by an upwelling of 4.5 Sv close to the western boundary, plus 1.2 Sv that enters across the equator.

The processes generating this annual mean picture are strongly seasonal. The cold inflow of Fig. 12a mostly occurs in summer. It rapidly mixes with warmer water to entrain outside of the 15°C temperature range near the western boundary—because mixing is also at a maximum in summer (not shown). This tends to increase the body of water with a temperature between 15° and 26°C. However, at the same time, water is being entrained upward across the 26°C isotherm to supply the net divergence of water above 26°C. This also occurs mainly in summer. The resulting upwelled water is then warmed by surface heating, through the following three seasons. Some of it escapes immediately across the equator in the Ekman transport. However, the rest of it returns via the recirculation to the western boundary the following summer. Here, this warmed water is available to mix with the intermediate temperature water created in the previous year, thus supplying heat absorbed at the surface to the deep inflow via a yearlong, two-step process.

c. Where does diapycnal mixing occur, and what is its cause?

It is useful to quantify the magnitude of "unphysical" FCT mixing compared to PP mixing. Figure 13a shows the depth of the 17°C isotherm at the end of Experiment 1 for the whole of the model region. Figure 13b shows the heat flux through this isotherm due to FCT at the end of this experiment. To obtain this quantity, the

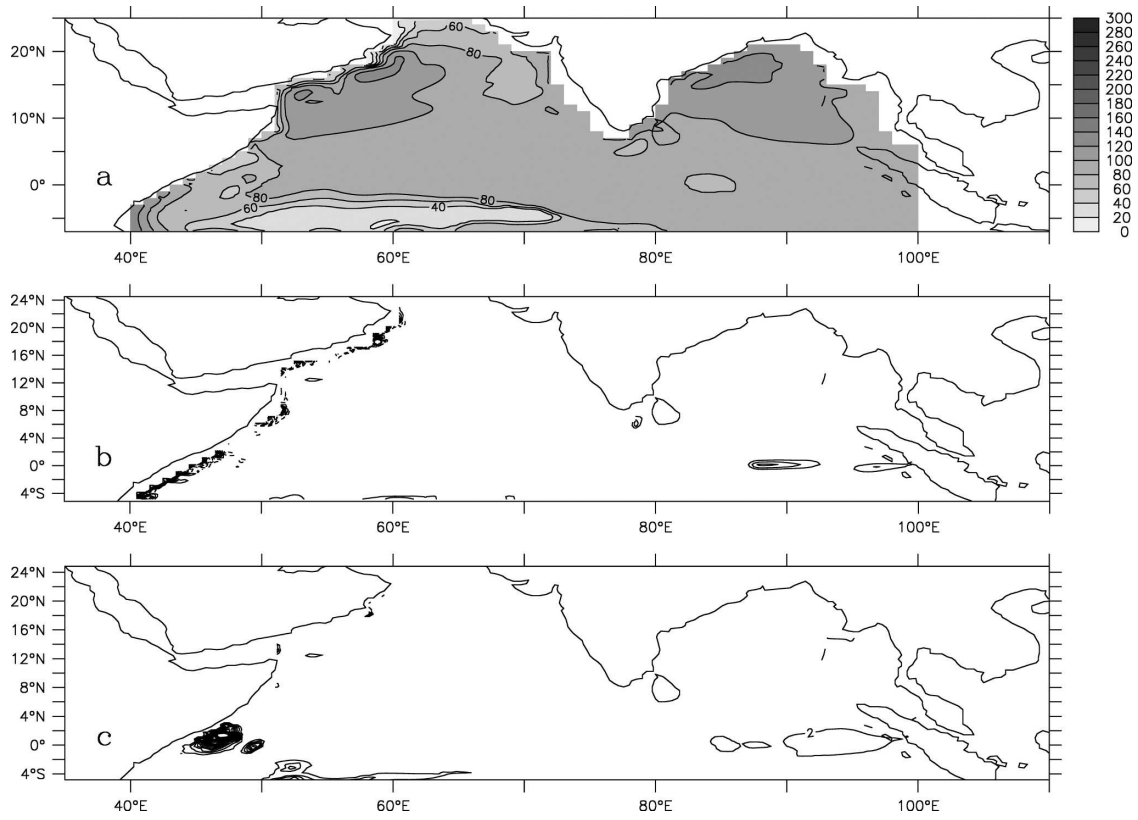

FIG. 13. (a) Depth of the 17°C isotherm (in m) at the end of the steady wind, steady swamp temperature run (experiment 1) and (b) the heat flux through this isotherm due to FCT, at the end of this experiment (contour interval: 10 W m^{-2}). (c) The heat flux through the 17°C isotherm due to the Pacanowski–Philander mechanism (contour interval: 2 W m^{-2}).

experiment was continued for a further 24 time steps, storing the output from every time step; the heat flux due to FCT can be calculated by differencing adjacent time steps (Griffies et al. 2000). FCT mixing occurs at only a few isolated locations for each time step; but, on average over 24 time steps, a clear pattern emerges, as can be seen in Fig. 13b. As seen in more detail in Fig. 11b, strong regions of mixing occur within one or two grid points of the western boundary both north and south of the equator. Some further mixing occurs in the region near 5°S, 45°–65°E; the 17°C isotherm is very shallow near here due to strong Ekman divergence in the region. The strong mixing at 85°–95°E along the equator is associated with a region where the rapid, shallow jet along the equator is slowing down [this can be seen in Fig. 9b, bearing in mind that this flow is confined above about 80 m (not shown)]. Maps similar to Fig. 13b have been obtained for each isotherm from 13° to 18°C; below 17°C the open-ocean occurrences of FCT mixing disappear, but FCT mixing still occurs all along the western boundary, at least down to 13°C. Qualitatively this mixing provides a causal mechanism for the fact that entrainment can be seen at all latitudes down to 12°C in Fig. 8a. However, it must again be emphasized that FCT mixing is a physically spurious mixing mechanism.

By contrast, Fig. 13c shows the heat flux through the 17°C isotherm due to the PP mechanism. The contour interval of 2 W m^{-2} is five times smaller than in Fig. 13b, so, except near the western boundary on the equator, PP mixing plays only a small role relative to FCT. It is still smaller at colder temperatures.

Figure 14 shows the area-integrated entrainment flux north of 5°S through isotherms as a function of their temperature, at the end of experiment 1, due to FCT (thick solid line), PP mixing (thin solid line), and their sum (long-dashed line). These have been calculated as $(1/\rho C_p)\partial Q/\partial T$ (see appendix A of Part I), where Q are the area integrals of heat fluxes like those in Figs. 13b,c. In steady state, the sum in Fig. 14 should be the same as the streamfunction in temperature coordinates at 5°S (short-dashed line). In fact, the streamfunction is substantially larger than the sum of the two mixing contributions. This is not too surprising in view of the ex-

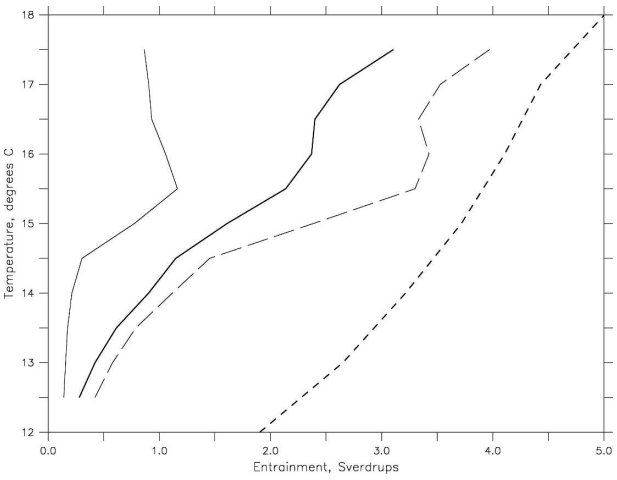

FIG. 14. Estimates of area-integrated entrainment flux, in Sv, north of 5°S at the end of experiment 1 as a function of temperature: FCT (heavy solid line), PP mixing (light solid line), and their sum (long-dashed line). The short-dashed line shows the overturning streamfunction in temperature coordinates at 5°S.

tremely "spiky" nature of the integrand, especially for FCT mixing (see Figs. 11b, 13b). It is thus more likely that the FCT contribution, rather than the PP contribution, has been underestimated. A study of snapshots from experiment 3 indicates that FCT mixing plays a very strong role in this case also.

d. How do nonlinear effects cause the horizontal streamfunction differences between the experiments?

The annual mean wind stresses used in generating each panel of Fig. 9 are identical, so the differences must be due to nonlinear and frictional effects in experiments 2 and 3 relative to the Sverdrup calculation. Initially neglecting friction, Godfrey (1973) and Kessler et al. (2003) treat the nonlinear terms in the depth-integrated momentum equations as "nonlinear stresses" (which can be obtained from model output). Taking the curl of these equations then results in a modified version of the Sverdrup relation with an extra term due to the curl of the nonlinear stress. Godfrey (1973) found that these curls were orders of magnitude larger than wind stress curls in Bryan and Cox's (1968) model western boundary current; they spun up vigorous eddies. Because zonal nonlinear stresses are large close to the equator but small elsewhere, Kessler et al. (2003) found that large, zonally oriented regions of extra curl can result. In the Pacific these cause major modifications to the "traditional" Sverdrup horizontal streamfunction when the modified Sverdrup relation is integrated westward from the eastern boundary.

The effects found by Godfrey (1973) and Kessler et al. (2003) are both apparent in Fig. 15, which shows the annual mean differences in the nonlinear stress curls in experiments 2 and 3 for year 6. Ignoring lateral friction, a "Sverdrup" streamfunction difference between these experiments must be calculable by integrating $(\rho\beta)^{-1}\text{curl}(\tau_{\text{NL3}} - \tau_{\text{NL2}})$ westward from the eastern boundary, in the familiar fashion. Here τ_{NLk} is the nonlinear stress from experiment k. However, even without doing this, it is readily seen that the curls of Fig. 15 are qualitatively right for generating the differences between Figs. 9b and 9c. Thus a patch of positive curl is seen near 7°N, 51°E with a negative patch near 7°N, 53°E, implying (through the modified Sverdrup relation) strong northward and southward difference flows, respectively. These are responsible for the greater strength of the Great Whirl in experiment 3 than experiment 2 (Figs. 9c,b). The strong positive curl difference near 0°, 48°E in Fig. 16 cancels the southward cross-equatorial return flow, seen in Fig. 9b but not in Fig. 9c. The small, zonally elongated patches of curl in the east Indian Ocean, of opposite sign across the equator, cause net meridional flow divergence away from the equator. This strengthens the eastward equatorial current in Fig. 9c compared to Fig. 9b. Note that—while it is true that the nonlinear stress differences "drive" the differences in western boundary eddies via the modified Sverdrup relation—it is also true that the nonlinear stresses are generated by the eddies. This blurring of cause and effect is to be expected from nonlinear stresses.

e. What sets the magnitude and temperature distribution of the Indonesian Throughflow?

The experimental domains used here and in Part I had flat bottoms and vertical walls, so the flows could be analyzed accurately for some months after the application of driving winds by use of a linearized version of the equations of motion in which a number of vertical modes develop independently (e.g., Gill 1982). As a result, upwelling north of the equator propagates Kelvin and Rossby waves along their usual paths north of 7°S—the northern boundary of the Indonesian Throughflow—lowering sea level there; but this effect can proceed no farther south. Thus, pressure differences develop as a function of depth across the Indonesian gap, driving a net throughflow via geostrophy. As in Part I, in the absence of nonlinearities, each mode will reach a Sverdrup equilibrium—with the result that all inflow replacing the Ekman outflow must occur within the surface mixed layer (McCreary 1980). Also as in Part I, diapycnal entrainment is the principal nonlinear mechanism stopping this from happening.

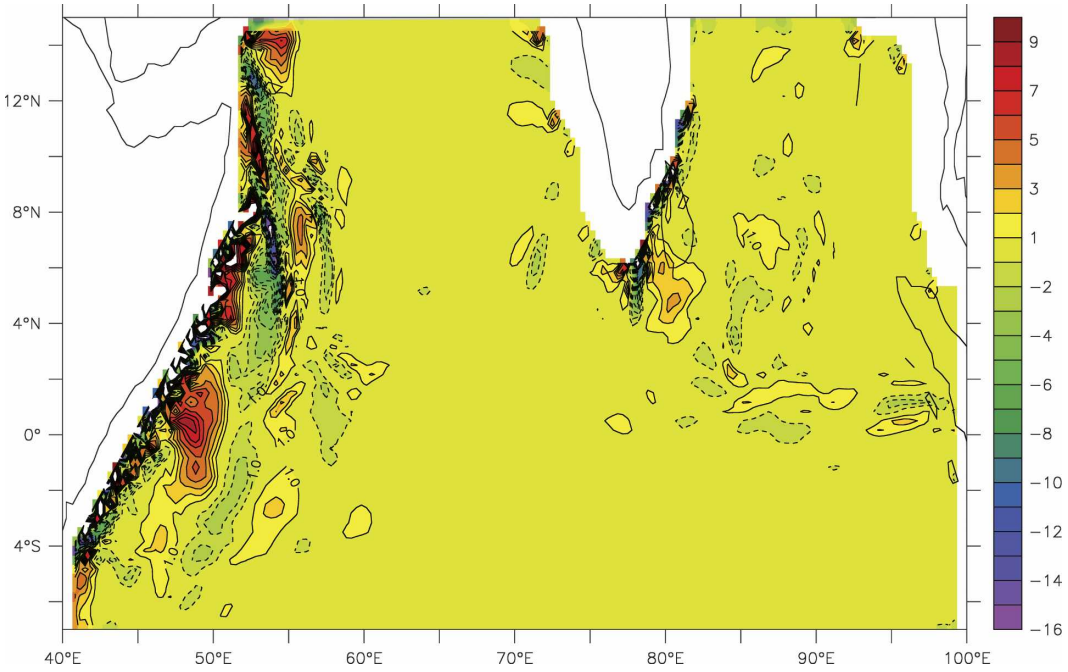

FIG. 15. Contours and shading show the curl of the difference between nonlinear stress vectors: expt 3 − expt 2.

As discussed in Part I, this entrainment may generate Kelvin and Rossby waves in much the same way that the wind stresses do, and waves from both entrainment and wind stress (regardless of whether or not the model entrainment is physically valid) are likely, in the model, to contribute to setting the final steady-state distribution of inflow through the Indonesian gap.

This raises the possibility that—at least in present model geometry—entrainment processes within the northern Indian Ocean can control the vertical profile of the Indonesian Throughflow (rather than the other way around). Spall (2003) explores a somewhat similar situation, inspired by entrainment/detrainment in the Leeuwin Current.

Unfortunately, it is not easy to distinguish between Kelvin waves driven by entrainment from those driven by winds since in summer the latter follows the former with a time lag of a month or so. We have been unsuccessful so far in clearly demonstrating that the entrainment along the model's Somali Current is generating Kelvin waves along the equatorial and eastern boundary waveguides.

5. Summary and discussion

The area-integrated AMNHFs from climatologies in Fig. 1 differ considerably among themselves, and the spread of OGCM heat fluxes is also fairly wide. It is only when several of both are assembled, as in Fig. 1, that the OGCM results seem systematically low compared to the climatologies. Motivated by Fig. 1, a series of experiments has been undertaken, ranging from ones with very idealized tropical Indian Ocean geometry and winds to reasonably realistic ones. The last—experiment 3 of this paper—has a realistic coastline shape, fully seasonal wind stresses, and a fully seasonal heat flux boundary condition, so (despite various defects) it is reasonable to compare results from it with others, such as those listed in Table 1 of Part I.

Our results suggest that many present-day OGCMs are at least potentially subject to serious errors in modeling diapycnal mixing, due either to coarseness of resolution or to spurious entrainment in corners in model coastlines, or both. The effects of coastline corners may be considerable. In particular, according to Fig. 12, mixing is distributed at a number of locations along the western boundary, so the analogy of the northwest eddy of Part I with the "Great Whirl" in this paper is not strong; but the coincidence of these locations with coastline steps suggests that model mixing may be a consequence of "steppiness" rather than real. The mixing problems also have the unfortunate effect that it would be unwise to use present models as a guide to interannual variations in SST caused by earlier interannual variations in deep mixing. Resolution of these issues requires more modeling research to settle the vari-

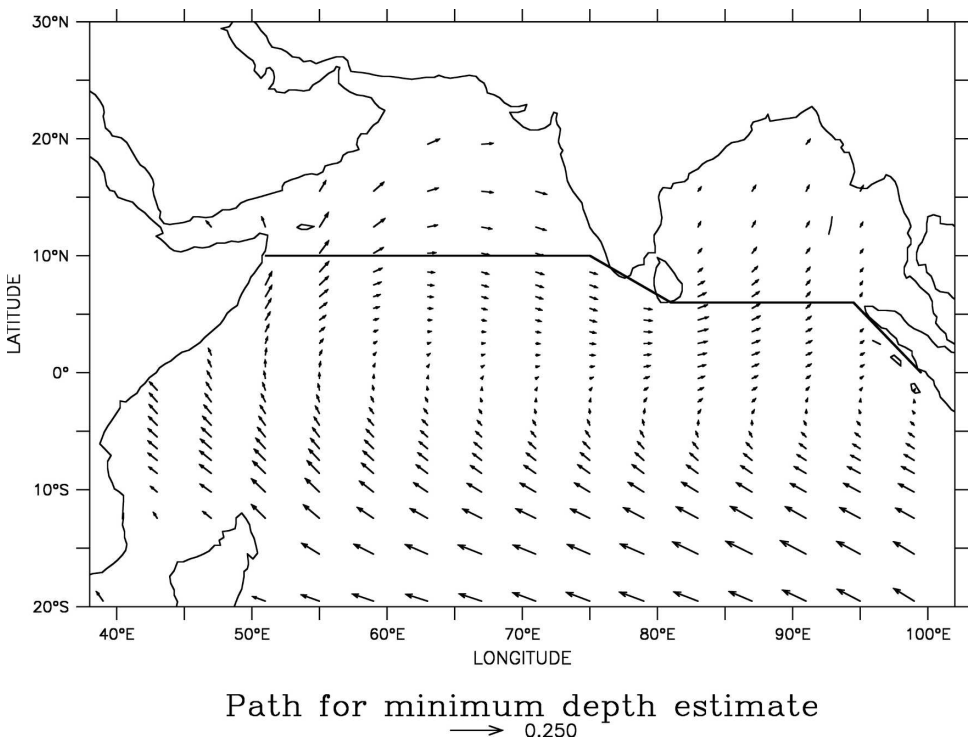

FIG. 16. The vectors show the annual mean wind stresses from the FSU dataset; scale vector is 0.1 N m^{-2}. The lines show the integration path used for the wind stress integration, described in the appendix, to obtain the depth-integrated steric height at the African western boundary.

ous unresolved questions. Use of density "layer" models should remove many of the problems encountered here—though high resolution in density would be necessary so that low Richardson number events can be explicitly modeled. For "level" models such as ours, T. McDougall (2006, personal communication) suggests that use of advection by the "temporal-residual-mean velocity" (TRM: McDougall and McIntosh 2001) can replace the unphysical mixing regions in the steps of model coastline topography with adiabatic, advective flows.

The results of Part I suggested that there is a substantial absolute minimum value of the area-integrated AMNHF into the tropical Indian Ocean comparable in magnitude to the average of all the OGCM values shown in Fig. 1. The revised "minimum depth" principle of this paper indicates that this minimum depth is more like 150 than 200 m and that the temperature above which flow must occur (if convective overturn at the western boundary is to be avoided) is more like 14.5° than 12.9°C, as in Part I. Thus Part I somewhat overestimated the minimum heat flux. However, the important point to note is that this principle—independent of mixing parameterization or grid spacing—implies that area-integrated AMNHF, heat transport, and mixing must be larger than a quite substantial minimum value, which must be exceeded even by models driven only with annual mean wind stresses.

Experiment 3 showed that, in the present model (as opposed to our unpublished coarse-resolution results), inclusion of seasonal wind stress variations resulted in a substantial increase in area-integrated AMNHF (cf. thick purple lines in Fig. 1). The difference between the OFES1 and OFES2 results in Fig. 1 shows that inclusion of daily winds/storms may further increase area-integrated AMNHF.

In all three main experiments of Part I, the mixing needed to supply that heat flux was generated in a Great Whirl–like feature independent of the mixing mechanism. The present results at least suggest that the mixing occurs near the African western boundary, but the "corner mixing" problems preclude a more definite conclusion. Recirculation in the western boundary flow is an essential part of the process of bringing water below minimum SST to the surface in both the present and earlier model.

The OFES2 model has much smaller coastline steps than the present model and is eddy permitting, so we look forward to analyzing its data to find when, where, by what mechanism, and why mixing events occur. If (at

least in such models) the mixing is physically realistic and storms are indeed essential contributors to the extra mixing and heat flux, the interesting possibility is raised that one year's "storminess" may affect a later year's SST. Storminess may thus be a predictor of climate variability in the monsoon region.

Acknowledgments. This paper emerged through a "trial and error" process, over 10 years. One of us (JSG) wishes to thank the other coauthors (and Dr. Linda Waterman and Ms. Yan-Li Zhang, coauthors of earlier, unsuccessful efforts) for their patience. We also wish to thank Professor Qinyu Liu, for making the visits of Zhang and Hu to Tasmania possible; and Drs. Stephen Griffies and Trevor McDougall, for help in identifying the model problems. This study was supported by a program from the National Natural Science Foundation of China (NSFC) under Grant 40576006.

APPENDIX

Calculation of a "Minimum Depth Current" Generated by Arbitrary (Steady) Wind Stresses in an Arbitrarily Shaped Basin

Here the minimum depth principle of Part I is adapted to apply in the more realistic model geometry and winds considered here. Only the response to steady winds in Fig. 1 is considered.

It is assumed—as is usual in, for example, analysis of World Ocean Circulation Experiment (WOCE) zonal sections—that the total northward flow through some latitude y, replacing a given southward Ekman flux across that latitude in a closed basin, is in geostrophic balance. If the western and eastern boundary walls at latitude y are vertical to a great enough depth that a "depth of no motion" Z can be used for estimating the side-to-side geostrophic flow, then (on multiplying both sides of the mass budget equation by Coriolis parameter f) one finds

$$g[P(x_E, y) - P(x_W, y)] = g\int_z^0 z[\Delta_W(z) - \Delta_E(z)]\,dz = \int_{x_E}^{x_W} \tau^{(x)}(x, y)\,dx, \quad \text{(A1)}$$

where P is the depth-integrated steric height defined in appendix B of Part I. Here $\Delta_E(y, z)$, $\Delta_W(y, z)$ are the specific volume anomaly (SVA) profiles at boundary points, such as the eastern and western boundaries of the Arabian Sea, or Bay of Bengal, or the entire Indian Ocean south of Sri Lanka.

As seen in Fig. 9, the Sverdrup relation appears to hold fairly well. Following Godfrey (1989), it is therefore assumed that values of depth-integrated steric height P along the east side of the Arabian Sea or Bay of Bengal satisfy

$$g\partial P/\partial l = \tau^{(l)}/\rho, \quad \text{(A2)}$$

which (on division by f) implies that offshore Ekman transport is supplied locally by onshore geostrophic flow. Here l represents alongshore distance (and direction). Integrating (10) along the west Indian coast yields

$$\rho g[P(x_E(y), y) - P(x_E(y_0), y_0)] = \int_{y_0}^{y} \tau^{(l)}(x_E(y), l)\,dl. \quad \text{(A3)}$$

Adding (A1) to (A3) gives

$$\rho g[P(x_E(y_0), y_0 - P(x_W, y))] = g\int_{-z}^{0} [\Delta_E(y_0, z) - \Delta_W(y, z)]\,dz = \int_{x_E}^{x_W} \tau^{(x)}(x, y)\,dx + \int_{y_0}^{y} \tau^{(l)}(x_E(y), l)\,dl. \quad \text{(A4)}$$

The path of this wind integral for the Arabian Sea is seen in Fig. 16, along with the annual mean wind stresses to be integrated along the path. Using similar arguments, (A4) can be extended along the two dashed lines farther east in Fig. 16, as well, to end at (0°, 100°E) off Sumatra. This yields

$$\rho g(P(0°, 100°E) - P(x_W, y)) = \rho g\int_{-z}^{0} z(1/\rho_E(y_0, z) - 1/\rho_W(y, z))\rho_0\,dz = \int_{(path)} \tau^{(l)}(x, y)\,dl, \quad \text{(A5)}$$

where (path) is the sum of the four lines shown in Fig. 16. For latitudes y south of Sri Lanka, the path consists of a zonal integral from Sumatra to Africa at latitude y plus an integral from 0 to y along the Sumatran coast.

Thus, knowing the density profile $\rho_E(0, z)$ at the single point (0°, 100°E) off Sumatra, a minimum depth $Z(y)$ can be evaluated at each latitude, using (B3) of Part I with the integral of wind stress along the path of Fig. 16 in place of $\rho f V$.

REFERENCES

Bryan, K., and M. D. Cox, 1968: A nonlinear model of an ocean driven by wind and differential heating: Part I. Description of the three-dimensional velocity and density fields. *J. Atmos. Sci.,* **25,** 945–967.

Da Silva, A. M., C. Young, and S. Levitus, 1994: *Algorithms and Procedures.* Vol. 1, *Atlas of Surface Marine Data 1994,* NOAA Atlas NESDIS 6, 83 pp.

Gill, A. E., 1982: *Atmosphere–Ocean Dynamics.* Academic Press, 662 pp.

Godfrey, J. S., 1973: Comparison of the East Australian Current with the western boundary current in Bryan and Cox's (1968) numerical model ocean. *Deep-Sea Res.,* **20,** 1059–1076.

——, 1989: A Sverdrup model of the depth-integrated flow for the world ocean allowing for island circulations. *Geophys. Astrophys. Fluid Dyn.,* **45,** 89–112.

——, G. C. Johnson, M. J. McPhaden, G. Reverdin, and S. E. Wijffels, 2001: The tropical ocean circulation. *Ocean Circulation and Climate,* G. Seidler, J. Church, and J. Gould, Eds., Academic Press, 215–246.

——, R.-J. Hu, A. Schiller, and R. Fiedler, 2007: Explorations of the annual mean heat budget of the tropical Indian Ocean. Part I: Studies with an idealized model. *J. Climate,* **20,** 3210–3228.

Griffies, S. M., R. C. Pacanowski, and R. W. Hallberg, 2000: Spurious diapycnal mixing associated with advection in a *z*-coordinate ocean model. *Mon. Wea. Rev.,* **128,** 538–564.

Haney, R. L., 1971: Surface boundary condition for ocean circulation models. *J. Phys. Oceanogr.,* **1,** 241–248.

Kessler, W. S., G. C. Johnson, and D. W. Moore, 2003: Sverdrup and nonlinear dynamics of the Pacific Equatorial Currents. *J. Phys. Oceanogr.,* **33,** 1027–1043.

Lee, T., and J. Marotzke, 1998: Seasonal cycles of meridional overturning and heat transport of the Indian Ocean. *J. Phys. Oceanogr.,* **28,** 923–943.

Legler, D. M., I. M. Navon, and J. J. O'Brien, 1989: Objective analysis of pseudostress over the Indian Ocean using a direct-minimization approach. *Mon. Wea. Rev.,* **117,** 709–720.

Levitus, S., 1982: *Climatological Atlas of the World Ocean.* NOAA Prof. Paper 13, 173 pp. and 17 microfiche.

——, 1987: Meridional Ekman heat fluxes for the World Ocean and individual ocean basins. *J. Phys. Oceanogr.,* **17,** 1484–1492.

McCreary, J., 1980: Modelling wind-driven ocean circulation. Hawaii Institute of Geophysics Rep. HIG-80-3, University of Hawaii at Manoa, Honolulu, HI, 64 pp.

McDougall, T. J., and P. C. McIntosh, 2001: The temporal-residual-mean velocity. Part II: Isopycnal interpretation and the tracer and momentum equations. *J. Phys. Oceanogr.,* **31,** 1222–1246.

Miyama, T., J. P. McCreary Jr., T. G. Jensen, J. Loschnigg, S. Godfrey, and A. Ishida, 2003: Structure and dynamics of the Indian Ocean cross-equatorial cell. *Deep-Sea Res. II,* **50,** 2023–2047.

Oberhuber, J. M., 1988: An atlas based on the COADS data set: The budgets of heat, buoyancy and turbulent kinetic energy at the surface of the global ocean. Max-Planck Institut für Meteorologie Rep. 15, 160 pp.

Pacanowski, R. C., 1995: MOM2 documentation user's guide and reference manual version 1.0. GFDL Ocean Tech. Rep. 3, 232 pp.

——, and S. G. H. Philander, 1981: Parameterization of vertical mixing in a numerical models of tropical oceans. *J. Phys. Oceanogr.,* **11,** 1443–1451.

Schiffer, R. A., and W. B. Rossow, 1983: The International Satellite Cloud Climatology Project (ISCCP): The first project of the World Climate Research Programme. *Bull. Amer. Meteor. Soc.,* **64,** 779–785.

Spall, M. A., 2003: Islands in zonal flow. *J. Phys. Oceanogr.,* **33,** 2689–2701.

Yu, L., R. A. Weller, and B. Sun, 2004: Improving latent and sensible heat flux estimates for the Atlantic (1988–1999) by a synthesis approach. *J. Climate,* **17,** 373–393.